

See discussions, stats, and author profiles for this publication at: <https://www.researchgate.net/publication/229159017>

Exploiting the Protein Corona around Gold Nanorods for Loading and Triggered Release

ARTICLE in ACS NANO · JULY 2012

Impact Factor: 12.88 · DOI: 10.1021/nn301389c · Source: PubMed

CITATIONS

50

READS

116

4 AUTHORS, INCLUDING:



[James Kah](#)

National University of Singapore

28 PUBLICATIONS 429 CITATIONS

SEE PROFILE



[Angel Zubieta](#)

University of Texas at Austin

2 PUBLICATIONS 67 CITATIONS

SEE PROFILE



[Kimberly Hamad-Schifferli](#)

University of Massachusetts Boston

53 PUBLICATIONS 2,263 CITATIONS

SEE PROFILE

Exploiting the Protein Corona around Gold Nanorods for Loading and Triggered Release

James Chen Yong Kah,^{†,*} John Chen,[†] Angel Zubieta,[§] and Kimberly Hamad-Schifferli^{†,*,‡,⊥,*}

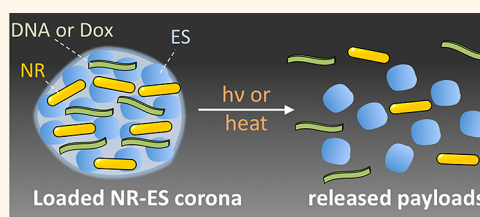
[†]Department of Biological Engineering and [‡]Department of Mechanical Engineering, Massachusetts Institute of Technology, Cambridge, Massachusetts 02139, United States and [§]Department of Biomedical Engineering, University of Texas at Austin, Austin, Texas 78712, United States. [⊥]Present address: MIT Lincoln Laboratory, 244 Wood Street, Lexington, Massachusetts 02420-9108.

Gold nanoparticles (NPs) have unique optical properties that are exploited for imaging,^{1–3} biosensing,^{4,5} photothermal therapy,^{6,7} triggered drug release,^{8–12} and numerous other biological applications.¹³ Because of their size, NP behavior is dominated by their surface, and surface modification strategies can enhance functionality, enable targeting, load drugs, and improve solubility and biocompatibility.^{2,14–17}

However, when NPs are introduced to biological fluids, they encounter high concentrations of proteins which nonspecifically adsorb to the NP, forming a multilayered “protein corona”.^{18,19} The protein corona is composed of numerous protein species that bind weakly and dynamically to the NP with a gradient of binding energies and thus has presented vexing challenges. These adsorbed proteins can completely mask the tailored surface, affecting NP cellular uptake, protein and cell interactions, and sometimes preventing receptor binding to ligands on the NP.^{20–26} Because biological behavior is now dominated by the protein corona, the NP identity is almost lost, where its material and surface chemistry play only a seemingly indirect role. There has been recent progress in its characterization,^{19,22,27–29} but results overwhelmingly show that protein corona behavior is difficult to predict and control.

Because corona formation around NPs is unavoidable, we believe it is imperative to strategically factor it into the design of the NP. Despite its tremendous complexity and potential for undesirable ramifications, the protein corona possesses beneficial properties that can be exploited. The very proteins that adsorb to the NP, the serum proteins, have been naturally designed for small molecule transport.^{30–32} Serum proteins are versatile and can solubilize either

ABSTRACT



We form coronas of serum proteins on gold nanorods (NRs) coated with cetyltrimethylammonium bromide (CTAB). These coronas can be exploited for their ability to hold small molecular therapeutics at a capacity much higher ($\sim 5\text{--}10\times$) than what covalent conjugation strategies can achieve. Coronas are loaded with DNA oligonucleotides and Doxorubicin, showing that they can hold species of either negative or positive charge. Payload capacity varies with assembly strategy, ionic strength, and loading concentration. Payload release can be achieved by increasing the temperature or by ultrafast laser excitation of the NRs at their longitudinal surface plasmon resonance. DNA leakage from the corona is minimal within the first 3 days of preparation, although Dox leakage was more significant. The coronas also stabilize the NRs in buffer and biological media. This study demonstrates the biological utility of the protein corona around nanomaterials, contrasting the common view of the corona as an undesirable biological response.

KEYWORDS: protein corona · gold nanorod · triggered release · nonspecific adsorption · serum proteins · oligonucleotide · Doxorubicin

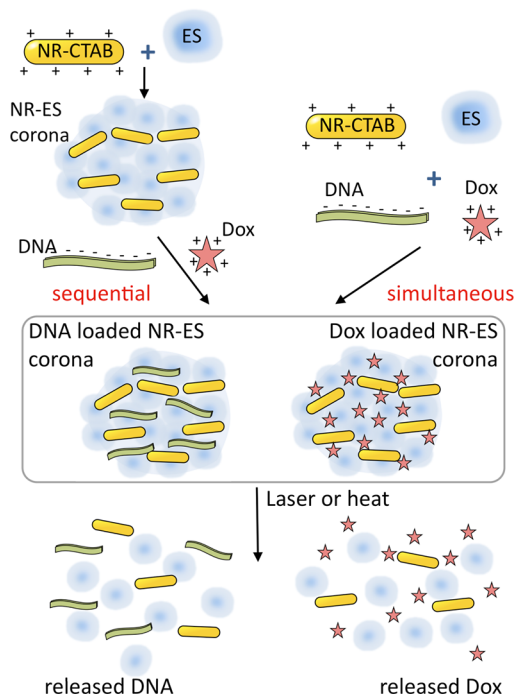
hydrophobic drugs or charged molecules^{33–39} and have been used to stabilize NPs against aggregation.^{40,41} Consequently, coronas around the NRs composed of serum proteins could potentially act as sponges with high payload capacity. In comparison, covalent coupling can hold one monolayer at maximum⁴² but is often less due to chemical coupling inefficiencies or surface effects such as intermolecular repulsion and steric hindrance. Therefore, moving beyond covalent strategies poses great opportunities for increasing NP payloads. Furthermore, coronas can help

* Address correspondence to schiffer@mit.edu, jameskah@mit.edu.

Received for review March 29, 2012 and accepted July 17, 2012.

Published online 10.1021/nn301389c

© XXXX American Chemical Society



Scheme 1. Formation of ES protein coronas on NR-CTAB and their loading with DNA and Dox payloads by simultaneous or sequential assembly. DNA and Dox can be released by heat or ultrafast laser excitation of the NRs.

stabilize NPs, which often suffer from aggregation in buffers and media.^{43,44} Finally, tuning corona properties could potentially enable controlling the NP biological fate^{45,46} and even disease state.^{47,48}

Here, we create coronas on cetyltrimethylammonium bromide coated gold nanorods (NR-CTAB) using serum proteins, which enhance their carrier properties for DNA oligonucleotides and the anticancer drug Doxorubicin (Dox), while also improving their stability (Scheme 1). Corona payload capacity exceeds amounts achieved by existing covalent strategies and eliminates the need for ligand exchange. NR optical properties enable light-triggered release of the payloads from the coronas. Instead of being an undesirable biological effect, we demonstrate that the protein corona can be beneficially exploited, thereby enhancing the properties of nanomaterials in biology.

RESULTS AND DISCUSSION

Corona Formation on NRs. NRs were chosen as the scaffold for the coronas because their tunable Near Infrared (NIR) absorption enables laser-triggered release.^{8–12,49,50} NR-CTAB with dimensions of 42.1 ± 0.4 nm by 11.7 ± 0.2 nm (aspect ratio = 3.6) and a longitudinal surface plasmon resonance (LSPR) at 800 nm (Figure 1a) were synthesized using established protocols.⁵¹ CTAB is known to limit NR stability, result in cytotoxicity, and induce aggregation in media.^{16,52,53}

We formed coronas on NR-CTAB by incubation with equine serum (ES), a commonly used cell culture

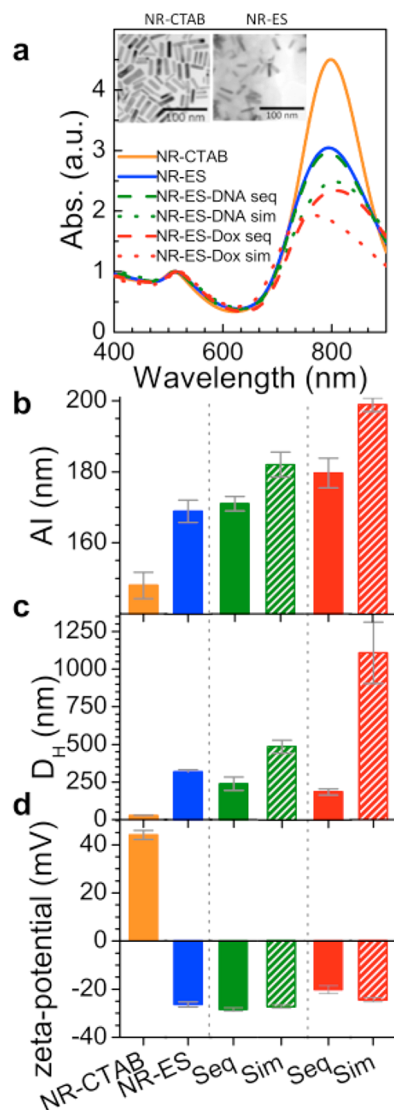


Figure 1. NR-ES characterization. (a) UV-vis of NR-CTAB (orange), NR-ES (blue), NR-ES-DNA by sequential (green dashed line) and simultaneous assembly (green dotted line), NR-ES-Dox by sequential (red dashed line) and simultaneous assembly (red dotted line). Inset, TEM of NR-CTAB and NR-ES; (b) aggregation index (AI) based on absorption spectra; (c) average D_H of NRs with ES and payloads measured by DLS; and (d) zeta-potential. Error bars based on standard error of triplicates.

serum. Corona formation did not change NR core size but resulted in a sparse agglomerate of proteins around the NRs (Figure 1a, inset). The LSPR of NRs with a corona of ES proteins (NR-ES) broadened, decreased in intensity, and blue-shifted 2.5 nm relative to NR-CTAB. LSPR position and width are sensitive to NR-NR interactions,^{44,54} and because these changes were small, they suggest ES induced slight NR clustering but not complete aggregation. The aggregation index (AI) was quantified based on the LSPR spectral changes, where higher AI values indicate lower stability.⁵⁵ NR clustering caused the AI to increase from 148 nm for NR-CTAB to 169 nm for NR-ES (Figure 1b). Hydrodynamic diameter (D_H) measured by DLS increased

from 26 ± 3.4 nm to 316 ± 14.9 nm (Figure 1c), suggesting that the corona is a large agglomerate containing several NRs. The zeta-potential of the NR-ES corona was -26.4 ± 1.07 mV, opposite in charge to NR-CTAB ($+44.1 \pm 1.88$ mV) because of the negative ES proteins (Figure 1d).⁵⁶ These results show that ES proteins formed a corona around NR-CTAB, altering its surface properties.

Two assembly approaches to load DNA and Dox onto NR-ES were used (Scheme 1). Sequential assembly involved forming the ES corona around NR-CTAB first, then adding payload. Simultaneous assembly involved adding ES and payload simultaneously to NR-CTAB. The loaded NR-ES LSPR broadened and decreased in intensity relative to NR-ES, suggesting that DNA and Dox loading destabilized the NRs (Figure 1a). Also for simultaneously assembled coronas for both payloads were higher than for sequential, suggesting that simultaneous assembly resulted in greater destabilization (Figure 1b). This is expected as simultaneous assembly allows a larger amount of ES protein to interact with both NR-CTAB and the payloads. We also observed a significant blue shift in the LSPR of simultaneously assembled NR-ES-Dox compared to the others. This is probably due to a higher degree of aggregation as confirmed from its AI, which resulted from a high concentration of both positive (Dox and free CTAB) and negative (ES) charged species interacting together.

The loading approach also affected NR-ES size. Both simultaneous DNA loading on NR-ES (NR-ES-DNA) and Dox loading on NR-ES (NR-ES-Dox) exhibited larger D_H values ($D_H = 487 \pm 43.6$ nm for DNA and 1109 ± 204.5 nm for Dox), while sequential loading resulted in a smaller $D_H = 238 \pm 44.3$ nm for DNA and 186 ± 21.4 nm for Dox (Figure 1c). Since tumor vessels are known to be leakier with large pore sizes, the large corona complex may be beneficial toward selective tumor targeting. The differences in D_H also suggest that the size of the NR-ES with payloads can potentially be tuned with appropriate assembly conditions.

NR-ES-DNA (sequential: -28.4 ± 0.73 mV and simultaneous: -27.2 ± 0.72 mV) were similar in charge to NR-ES (-26.4 ± 1.07 mV, Figure 1d). NR-ES-Dox was less negative (sequential: -20.2 ± 1.60 mV and simultaneous: -24.4 ± 0.92 mV) than NR-ES (-26.4 ± 1.07 mV) due to Dox's positive charge. For both payloads, the two assembly approaches resulted in small differences in surface charge, which could be due to differences in spatial distribution of the payloads within the corona.

Coronas Have High Capacity for Payloads. Next, we quantified the amounts of DNA and Dox on NR-ES. Quantification of thiol-modified payloads is typically achieved by competitive displacement using small molecule thiols such as mercaptohexanol (MCH).^{57,58} Surprisingly, a high concentration of MCH was unable to fully

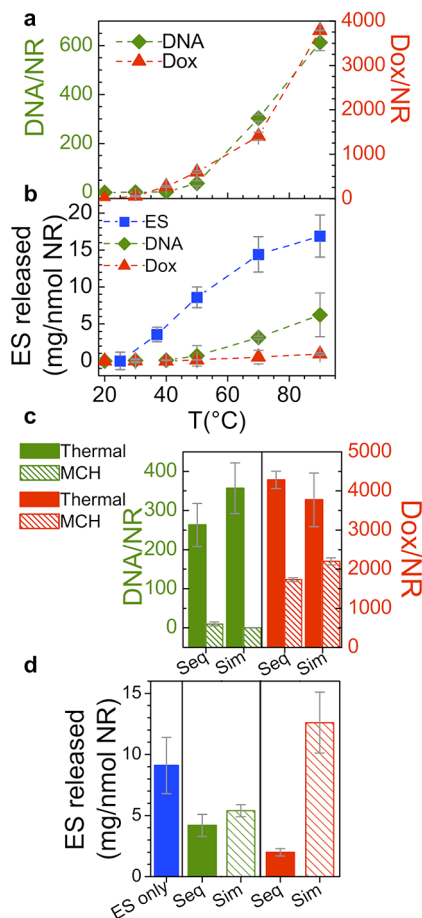


Figure 2. Quantifying the payloads and ES proteins on NR-ES from thermal release. (a) Thermal release of DNA (green diamonds) and Dox (red triangles) as a function of temperature. (b) ES proteins released from NRs with (green diamonds, red triangles) and without DNA/Dox (blue squares) as a function of temperature. (c) Thermal release at 90 °C for 30 min (solid bars) to obtain DNA and Dox loading by sequential and simultaneous assembly and release by MCH displacement (hashed bars). (d) Adsorbed ES proteins on NRs without (blue) or with DNA (green) and Dox (red) in NR-ES coronas prepared by sequential (solid) and simultaneous (hashed) assembly. Error bars based on standard error of triplicates.

displace ES and payloads from the NRs, resulting in displacement of only 10 DNA/NR for sequential assembly and 0.3 DNA/NR for simultaneous (hashed bars, Figure 2c). This could be due to the corona sterically blocking MCH from the NR surface, which suggests that the coronas greatly stabilize the NRs. Payload can also be quantified by loss of free DNA or Dox in the supernatant due to NR binding, but this tends to be inconsistent and unreliable due to the small differences in the measured total and free molecules.

Consequently, we utilized thermal treatment to release payloads from the NR-ES. Both DNA and Dox supernatant fluorescence increased with temperature (Figure 2a) and was accompanied by ES release (Figure 2b, green and red). Evidently, high temperature was able to disassemble the corona to release both ES and DNA or Dox into the supernatant. We quantified

released payload by standardizing exposure to $T = 90^\circ\text{C}$ for 30 min to allow comparison between samples. Further increases in heating time did not cause further increases in payload release amount (data not shown). This approach is somewhat limited due to the fact that the amount released was not the entire corona and thus probably underestimates actual loading. However, heating conditions were kept identical to keep the results consistent.

The DNA payload was 357 ± 64.6 DNA/NR for simultaneous assembly and 263 ± 54.7 DNA/NR for sequential (quantified from thermal treatment at $T = 90^\circ\text{C}$ for 30 min) (solid bars, Figure 2c). Electrostatic repulsion between the negative DNA and ES proteins probably hinders DNA binding to NR-ES in sequential assembly, resulting in lower loading. There were also more ES proteins on the NRs for simultaneous assembly (5.44 ± 0.50 mg/nmol NR) than sequential (4.24 ± 0.89 mg/nmol NR, Figure 2d), so simultaneous assembly probably involves residual CTAB mediating repulsion. In comparison, covalent attachment strategies using thiolated single-strand DNA can optimally achieve coverages of only 80–130 DNA/NR for similarly sized NRs (10 nm \times 40 nm).^{24,50} Furthermore, covalent strategies have an upper limit to the number of DNA that can be attached, which is 1 monolayer or ~ 109 DNA/NR for the NRs here.⁵⁹ This shows that the corona has $\sim 2\text{--}3\times$ higher DNA capacity than monolayer functionalization.

Quantification of Dox loading on NR-ES showed that sequential assembly could load 4282 ± 220 Dox/NR and simultaneous assembly 3773 ± 687 Dox/NR (Figure 2c). This suggests that alternating “layers” of the negative ES and positive Dox is beneficial, similar to layer-by-layer strategies on flat and NP surfaces.^{60,61} Compared to DNA, Dox loading was much higher ($\sim 13\times$), most likely due to Dox being smaller than DNA and because it is opposite in charge to the ES. Previous studies that load thiolated Dox onto gold NPs have achieved a monolayer loading, which would be 533 Dox/NR assuming the same Dox footprint for NPs and NRs.^{62,63} Thus, coronas can load $7\text{--}8\times$ more Dox than covalent attachment strategies.

For a fixed ES concentration during corona formation, fewer ES proteins were bound to NRs in the presence of DNA (sequential: 4.24 ± 0.89 mg/nmol NR, simultaneous: 5.44 ± 0.50 mg/nmol NR) than without (9.07 ± 2.28 mg/nmol NR, Figure 2d). This indicates that DNA and ES bind competitively to the NR. For Dox, the amount of ES on the NRs was 2.03 ± 0.26 mg/nmol NR for sequential assembly but 12.60 ± 2.54 mg/nmol NR for simultaneous. This suggests that Dox recruits ES to adsorb on NR-CTAB simultaneously. Conversely, excess unbound ES was removed during sequential assembly before Dox loading, resulting in less ES.

These results show that the coronas have a high capacity for DNA and Dox loading. However, we note that variability in loading is high. Error bars in the payload quantities were large, especially compared to covalent attachment strategies.²⁴ We believe this is due to the complex and random nature of corona formation involving noncovalent interactions between multiple species.

Tuning Payload Capacity. Next, conditions for varying the corona payload capacity were examined. Because electrostatic interactions are largely responsible for corona assembly and loading, charge screening is expected to affect payload amount. We varied phosphate buffer concentration ([PhB]) in assembly and measured the effect on loading for fixed DNA/NR and Dox/NR incubation ratios. DNA loading increased to 658 ± 32 DNA/NR at [PhB] = 5 mM (filled diamonds, Figure 3a). For [PhB] > 5 mM, loaded DNA decreased gradually to 270 ± 87 DNA/NR at [PhB] = 100 mM. This shows that ionic strength strongly influences DNA loading on NR-ES, and that an optimal [PhB] exists. This nonmonotonic dependence on ionic strength has been observed for electrostatic adhesion of bacteria to NPs⁶⁴ and protein–polyelectrolyte complexes where the Debye screening length at 5 mM PhB is approximately the size of the protein and thus salt screens electrostatic repulsion.^{65,66} NR-ES-DNA AI increased with [PhB] (open diamonds), indicating that the NRs were less stable. Although ionic strengths of 5–10 mM slightly compromised stability, the loading is $\sim 5\times$ higher than what is typically obtained for thiol-modified DNA. Thus, tuning [PhB] can balance stability with loading capacity.

Dox loading increased to 5444 ± 458 Dox/NR at 5 mM PhB (filled triangles, Figure 3b). Unlike for DNA, Dox loading remained relatively constant at ~ 5000 Dox/NR for [PhB] > 5 mM, showing that Dox loading was less sensitive to ionic strength. However, the AI for NR-ES-Dox also increased with [PhB] (open triangles, Figure 3b), indicating that stability decreased in a manner similar to NR-ES-DNA. Thus, by varying [PhB], Dox loading could be optimized to achieve $\sim 10\times$ higher than covalent attachment strategies.

The amount of ES adsorbed on the NRs without payload peaked at [PhB] = 5 mM (19.43 ± 2.73 mg/nmol NR) and then decreased with increasing [PhB], showing that [PhB] strongly influences corona formation (filled squares, Figure 3c). With DNA or Dox loaded on NR-ES, the amount of ES adsorbed varied with [PhB] in the same manner but was lower than in the absence of payload (Figure S1, Supporting Information).

We examined how varying payload/NR incubation ratios affected loading. DNA loading increased with DNA/NR incubation ratio to 444 ± 95 DNA/NR at the highest ratio (filled diamonds, Figure 3d). This shows that simply increasing DNA concentration during assembly increases DNA loading. AI decreased from

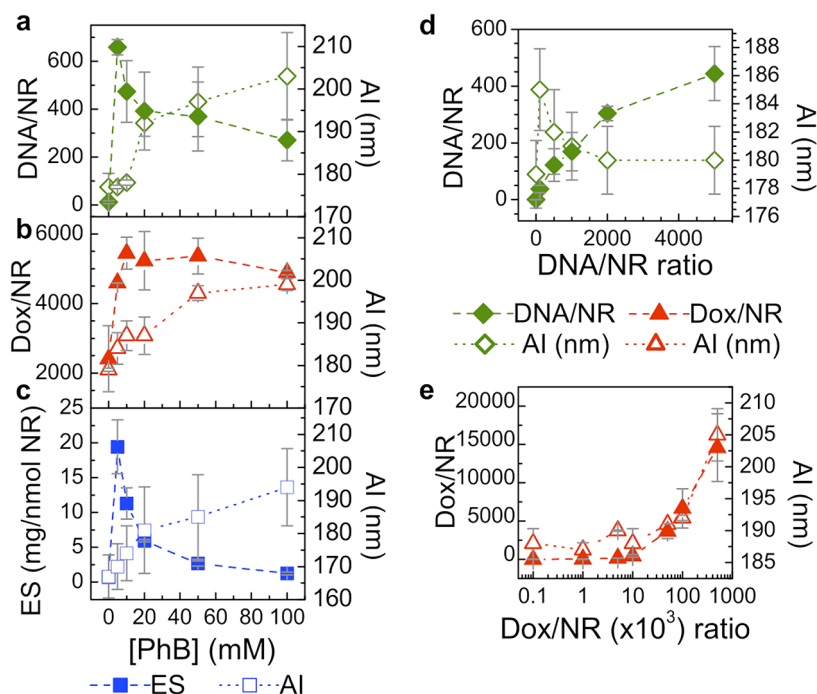


Figure 3. Dox and DNA loading as a function of ionic strength and payload/NR incubation ratios. (a) DNA loading (green filled diamonds) and AI (green open diamonds) as a function of [PhB] at DNA/NR incubation ratio of 2000:1. (b) Dox loading (red filled triangles) and AI (red open triangles) as a function of [PhB] at Dox/NR incubation ratio of 10^5 :1. (c) ES protein loading (blue filled squares) and AI (blue open squares) on NRs as a function of [PhB]. (d) DNA loading (green filled diamonds) and AI (green open diamonds) as a function of DNA/NR incubation ratio at [PhB] = 10 mM. (e) Dox loading (red filled triangles) and AI (red open triangles) as a function of Dox/NR incubation ratio at [PhB] = 10 mM. Error bars based on standard error of triplicates.

185 to 180 nm when the incubation ratio increased from 100 to 5000:1 (open diamonds), suggesting that DNA loading slightly stabilized the NRs.

Dox loading also varied with Dox/NR incubation ratio but exhibited a slightly different profile (filled triangles, Figure 3e). Only a small fraction of Dox (<400 Dox/NR) was loaded until the Dox/NR incubation ratio reached 10^4 :1, beyond which Dox loading increased to $1.46 \pm 0.44 \times 10^4$ Dox/NR. The corona's high capacity for Dox was most likely due to the small size and positive charge of Dox. NR-ES-Dox AI remained relatively unchanged at ~ 190 nm for low incubation ratios but increased to 205 nm at the highest ratio (5×10^5 :1, open triangles, Figure 3e). Unlike DNA, destabilization occurred at very high Dox loadings. DNA and Dox loadings were also quantified in terms of loading efficiency (Figure S2, Supporting Information).

The amount of ES proteins in the corona also varied with payload/NR incubation ratio, where more payload resulted in less ES (Figure S3, Supporting Information). Evidently, the payloads and ES proteins bind competitively to the NRs.

Laser-Triggered Release of Payloads. We investigated whether NR-ES could be triggered to release their payloads by ultrafast laser irradiation of the NR. Laser excitation at 800 nm melts the population of NRs that absorb at 800 nm to form spheres, causing the LSPR to decrease and blue shift, thus confirming NR melting

(Figure S4, Supporting Information).^{8,67,68} The subsequent payload release could be a result of corona reorganization around the NRs as they are melted, the denaturation of the adsorbed serum proteins in proximity to the heated NRs, or a combination of both effects. For DNA-loaded NR-ES, released DNA increased with irradiation time, reaching 155 ± 44 DNA/NR by 15 min (Figure 4a). Released amounts of DNA from the corona were higher than what has been achieved previously for covalent loading, which was ~ 90 DNA/NR for similarly sized NRs.⁸ Laser irradiation released much less DNA than thermal release (Figure 2a). This is most likely due to the fact that laser excitation heats an area of only ~ 10 nm around the NR (at $T > 100$ °C⁶⁹), which is much smaller than the corona size ($D_H \sim 300$ nm). Thus, heat generated by the NRs from ultrafast irradiation is not sufficient to heat the entire corona uniformly.

Laser irradiation was also able to release Dox from NR-ES-Dox. Released Dox amounts increased with irradiation time, reaching 593 ± 6 Dox/NR after 15 min (Figure 4b). High Dox release was also observed from Dox loaded on hollow gold nanospheres coated with chemically modified polyethylene glycol instead of a naturally occurring protein corona.⁷⁰ DNA and Dox release were also quantified in terms of release efficiency ($= \# \text{ released}/\text{total loaded on NR} \times 100\%$, Figure S5, Supporting Information).

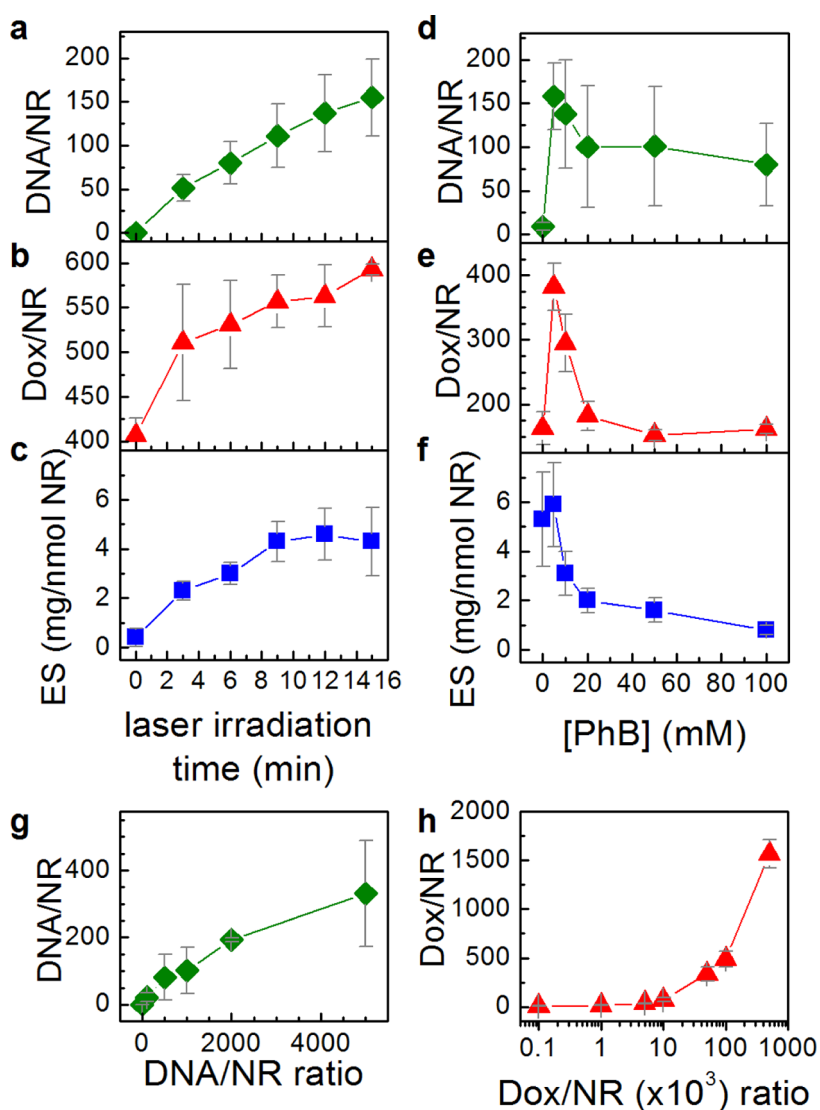


Figure 4. Release of DNA and Dox by laser excitation of the NRs in the coronas. (a) DNA, (b) Dox, and (c) ES protein release as a function of laser irradiation time. Laser-triggered release as a function of [PhB] for (d) DNA at a fixed DNA/NR incubation ratio of 2000:1. (e) Dox at a fixed Dox/NR incubation ratio of 10^5 :1, and (f) ES protein. Laser-triggered release at [PhB] = 10 mM of (g) DNA as a function of DNA/NR incubation ratio and (h) Dox as a function of Dox/NR incubation ratio. Error bars based on standard error of triplicates.

The payloads were still functional after triggered release from the coronas, where DNA was able to hybridize to its complement for simultaneous assembly. The hybridization curve (Figure 5, filled diamonds) is similar to that of plain DNA with its complement (control, open diamonds), indicating that the DNA can form a hybrid. While the sigmoidal shape is not identical, the curves still show approximately the same melting temperature.

In the absence of payload, NR melting was accompanied by corona disruption and release of ES proteins. Released ES increased to 4.56 ± 1.06 mg/nmol NR after 12 min, after which there was no additional release (Figure 4c). In the presence of payloads, the released ES was generally reduced and depended on the assembly approach (Figure S6, Supporting Information).

Triggered Release as a Function of Ionic Strength. We probed the effect of [PhB] on the amount of payload released by laser excitation for fixed DNA/NR and Dox/NR incubation ratios. The amount of released DNA varied with [PhB], peaking at 158 ± 22 DNA/NR at 5 mM PhB (Figure 4d), and had a similar profile to loading (Figure 3a). This suggests that lower ionic strength results in optimal DNA loading and also laser-triggered release. Laser release of Dox also peaked at 382 ± 37 Dox/NR at 5 mM PhB but decreased to 162 ± 8 as [PhB] was increased to 100 mM (Figure 4e). The Dox release profile with [PhB] differed from the loading profile (Figure 3b). Evidently, Dox release is sensitive to ionic environment, while its loading is not. In the absence of payload, laser-triggered release of corona proteins from NRs also peaked at 5 mM PhB (5.9 ± 0.1 mg/nmol NR) and then

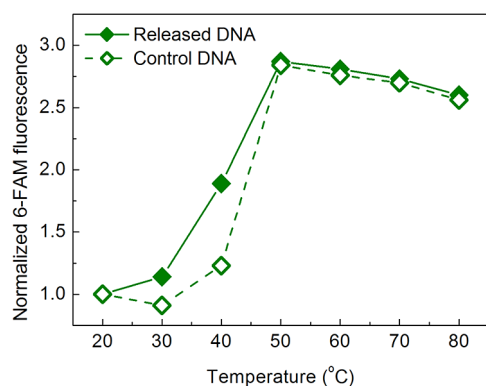


Figure 5. Functionality of the laser-triggered released payload. Melting curve of released DNA hybridized to its complement with a quencher (filled diamonds) compared to control DNA (open diamonds), demonstrating that the released DNA from the NR-ES-DNA was able to hybridize to its complement.

decreased with increasing [PhB] (Figure 4f). With payload present, the amount of ES proteins released by the laser was lower across all [PhB] (Figure S1b, Supporting Information), as was observed for loading, again confirming competitive binding.

Triggered Release as a Function of Payload/NR Incubation Ratio. The amount of laser-triggered released payload was measured as a function of the payload/NR incubation ratio during corona formation. The amount of released DNA increased with DNA/NR incubation ratio, reaching a maximum of 331 ± 91 released DNA/NR at a ratio of 5000:1 (Figure 4g). This was similar to the loading profile (Figure 3d) and confirms that a greater loading of DNA increases release amounts.

Laser-triggered release of Dox also increased with Dox/NR incubation ratio (Figure 4h). Release was not significant (<100 Dox/NR) for Dox/NR incubation ratios $<10^4$:1 but reached 1567 ± 148 Dox/NR at a ratio of 5×10^5 :1. Like DNA, the laser release profile was similar to the loading profile (Figure 3e). Laser-triggered release of both payloads was accompanied by ES protein release, which was generally lower with increasing payload incubation, as less ES proteins were adsorbed on the NRs (Figure S3, Supporting Information). These results show that the amount of DNA or Dox released by NR laser excitation can be tuned by simply changing [PhB] or the payload/NR incubation ratio.

Payload Leakage. Because payloads are bound to the NR-ES noncovalently, where many of the proteins bind weakly, payload leakage could potentially undermine the corona's ability to retain therapeutic molecules. Thus, we investigated payload leakage kinetics over 14 days for both assembly approaches at $T = 25^\circ\text{C}$. Initially DNA leakage was low (<30 DNA/NR, Figure 6a). This lag in leakage shows that the corona can be stably maintained for 3 days. Afterward, leakage increased and was faster for sequentially assembled coronas. After 14 days, 273 ± 69 DNA/NR had leaked out of NR-ES for sequential assembly and 121 ± 41 DNA/NR

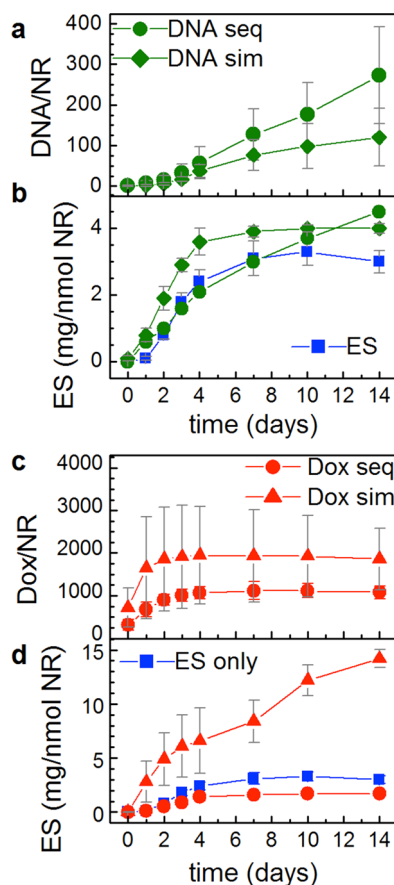


Figure 6. Payload leakage kinetics at $T = 25^\circ\text{C}$ and $[\text{PhB}] = 10\text{ mM}$. (a) DNA leakage from NR-ES-DNA coronas formed by sequential (green circles) and simultaneous assembly (green diamonds). (b) Leakage of ES from NR-ES (blue squares) or NR-ES-DNA coronas formed by sequential (green circles) or simultaneous assembly (green diamonds). (c) Dox leakage from NR-ES-Dox coronas formed by sequential (red circles) and simultaneous assembly (red triangles). (d) ES proteins leakage from NR-ES (blue squares) and NR-ES-Dox coronas formed by sequential (red circles) and simultaneous (red triangles) assembly. Error bars based on standard error of triplicates.

for simultaneous assembly. This shows that with time leakage can be significant. Because sequential assembly appeared to be less robust against leakage, it suggests that the DNA was probably distributed more toward the corona periphery. Leakage was also quantified in terms of percentage ($= \# \text{ payload leaked/total payload} \times 100\%$, Figure S7, Supporting Information).

Dox leakage was initially more significant, reaching 905 ± 65 Dox/NR (sequential assembly) and 1858 ± 704 Dox/NR (simultaneous) after 2 days (Figure 6c). Afterward, leakage slowed and saturated at day 4. The Dox could have initially leaked from the “soft” corona as it reorganized in the first few days, and the leakage stabilized with time when only a small amount of Dox could have leaked from the “hard” corona.²² The loading of Dox in the hard corona could have formed a stable complex that was not prone to leakage. After

14 days, 1122 ± 118 Dox/NR (sequential assembly) and 1954 ± 662 Dox/NR (simultaneous assembly) leaked.

Apparently, Dox is more prone to leakage due to its smaller size. Despite the larger amount of Dox leakage compared to DNA, the percentage that leaked was about half of DNA's (Figure S7, Supporting Information). Simultaneous assembly of Dox on NR-ES was less robust to leakage, probably due to a larger and looser corona formed. Therefore, sequential assembly of Dox is not only more stable in aqueous media but also able to load and retain more Dox.

Payload leakage was accompanied by ES leakage. Without payload, ES leakage was initially low and saturated at 3.12 ± 0.52 mg/nmol NR after 4 days (Figure 6b). Simultaneous DNA loading increased ES leakage to 3.87 ± 0.17 mg/nmol NR. Sequential loading resulted in a linear leakage response, reaching 4.50 ± 0.49 mg/nmol NR. Thus, DNA loading caused the corona to be more facile toward leakage. Dox loaded sequentially reduced ES leakage (1.71 ± 0.16 mg/nmol NR, day 14, squares, Figure 6d), while simultaneous assembly resulted in higher leakage (14.2 ± 0.82 mg/nmol NR, day 14, triangles), but the disparity is probably due to differences in the amount of adsorbed ES. Evidently, charged payloads disrupt the ES corona stability, making them more prone to leakage. Because the proteins in a corona are thought to form both a hard corona and a soft corona around NPs,²² location of the payload most likely influences the amount of leakage.

Stability. Another desirable consequence of corona formation is improved stability, especially for NR-CTAB which are known to aggregate in buffer and biological media, thus compromising utility.^{16,71,72} We investigated stability in $1 \times$ phosphate buffer saline (PBS) and RPMI 1640 cell culture media, which are both commonly used in cell culture for numerous cell lines. NR-CTAB aggregated in both $1 \times$ PBS and RPMI 1640, and its AI increased from 154 nm in water to 205 nm in $1 \times$ PBS and 233 nm in RPMI 1640 (orange, Figure 7). NR-ES AI was 177 nm in water due to NR clustering but decreased to 160 nm in $1 \times$ PBS and 164 nm in RPMI 1640, demonstrating that corona formation improved NR stability. Similarly, NR-ES with payloads by both assembly approaches showed negligible AI increases in $1 \times$ PBS and RPMI 1640. Additionally, corona

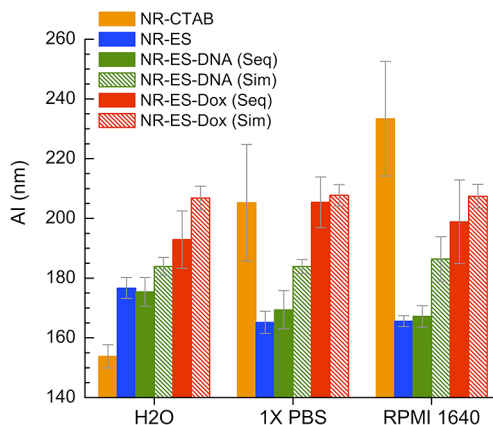


Figure 7. Stability of NR-ES coronas with and without payload. AI (aggregation index) of NR-CTAB (orange), NR-ES (blue), NR-ES-DNA (green), and NR-ES-Dox (red) in water, $1 \times$ PBS, and RPMI 1640 cell culture media. Error bars based on standard error of triplicates.

formation on NR-CTAB improved stability in repeated centrifugation (data not shown). It is known that CTAB can come off the NR surface, which causes NR aggregation and cytotoxicity.^{52,73,74} Complete removal of CTAB by ligand exchange can be difficult to achieve, so corona formation is a simple alternative that apparently acts as an effective overcoating or cloak, as has been observed for polyelectrolytes.⁷⁵

CONCLUSIONS

This study demonstrates that protein coronas around NRs can improve their carrier properties. The corona acts like sponge with a high capacity to hold small therapeutic molecules and can be utilized on both positive and negative species. Furthermore, the NR optical properties allow payload release in a remotely controlled manner. Environmental conditions such as ionic strength, payload/incubation ratio, and assembly strategy can optimize loading, laser-triggered release, and stability. DNA leakage was minimal for 3 days, although Dox leakage was more significant. While we still do not fully understand the properties and consequences of protein coronas, we hope that this demonstrates that they can be used beneficially. As we uncover more about protein coronas, eventually their design and optimization will enhance numerous biological applications.

MATERIALS AND METHODS

Synthesis and Characterization of Gold NRs. NR-CTAB were synthesized by non-seed-mediated growth.⁵¹ NR size was determined by transmission electron microscopy (TEM). The NR-CTAB were washed once by centrifuging at 12 000 rpm for 30 min to remove excess reactants, resuspended in Milli-Q water, and kept at room temperature before further experiments. The NR-CTAB concentration was determined from the UV-vis spectrum (Cary 100 UV-vis spectrophotometer, Agilent Technologies)

and known extinction coefficients.^{8,16} NR concentration in the experiments was ~ 1.5 nM.

Assembly of Protein Coronas with Payloads on NRs. Protein coronas with payload were assembled on NR-CTAB using two approaches. The first is a sequential approach, where the corona was formed on NR-CTAB first before the payloads were added. To form the protein corona, 1 mL of NR-CTAB was centrifuged at 12 000 rpm for 30 min before adding 1 mL of 0.4% equine serum (ES) (ATCC, Inc.) in 10 mM phosphate buffer (PhB, pH 7.4) directly

to the pellet and incubating it for 6 h at 37 °C. The NR-ES were washed once with buffer to remove excess protein, followed by the addition of the payload. The second is a simultaneous approach where both the 0.4% ES and payload in 10 mM PhB were added simultaneously to NR-CTAB, followed by overnight incubation at 37 °C.

The first payload is a negatively charged 20-mer DNA oligonucleotide with the following sequence: 5'-CAG CGT GCG CCA TCC TTC CC-3' (MW = 6559.4, Integrated DNA Technologies, Inc.). The 3' end of the DNA is attached to a FAM probe. The second payload is a positively charged Doxorubicin (Dox), an anticancer drug (MW = 579.98, Sigma-Aldrich Co.). Both DNA and Dox were added to NR-ES in final concentrations of 2 and 100 μ M, respectively.

NR-ES with payloads (NR-ES-DNA or NR-ES-Dox) were characterized for their morphology in TEM. We probed the change in the absorption spectrum, hydrodynamic diameter (D_h) using dynamic light scattering (DLS) (DynaPro Titan, Wyatt Technology Corporation), as well as zeta-potential (Malvern Zetasizer Nano ZS90) for the corona and payloads assembled on the NR-CTAB.

Quantifying Payloads on NR-ES. The amount of loaded DNA and Dox were quantified by measuring their fluorescence after releasing them from the NRs by a thermal release process. This involved heating 100 μ L of 1 nM NR-ES-DNA/Dox solution in a water bath at 90 °C for 30 min, and the solution turned purplish red to indicate the onset of NR aggregation as the corona and payloads were released. NR-ES-DNA/Dox were then centrifuged at 11 000 rpm for 10 min to isolate the fluorescent payload and ES proteins in the supernatant from the NR pellet. The ES proteins were quantified by measuring their intrinsic tryptophan fluorescence (λ_{ex} = 285 nm, λ_{em} = 343 nm) against known standards (see fluorescence spectrum of ES proteins in Figure S8, Supporting Information). While fluorescence quantitation is limited to species containing aromatic residues (e.g., tryptophan) in the media, we were able to obtain a linear fluorescence calibration curve with known concentration of ES. DNA was quantified by measuring the fluorescence of 6-FAM fluorescein tag (λ_{ex} = 495 nm, λ_{em} = 518 nm), and the Dox was quantified by measuring its intrinsic fluorescence (λ_{ex} = 480 nm, λ_{em} = 592 nm). It is important to note that while the pH sensitivity of 6-FAM fluorescence can be eliminated by dispersing NRs and DNA in PhB buffer (pH 7.4), 6-FAM is also sensitive to both the PhB and protein concentration in the supernatant (Figure S9, Supporting Information). We eliminate this sensitivity by obtaining the DNA calibration curve from suspending DNA in the relevant concentration of PhB and ES proteins found earlier. Fluorescence of ES proteins and Dox were not affected by PhB concentration, as well as the presence of each other and 6-FAM.

[PhB] in corona assembly and washing was varied from 0 to 100 mM at fixed DNA/NR and Dox/NR incubation ratios of 2000:1 and 10⁵:1, respectively. DNA/NR incubation ratio was varied from 0 to 5000:1, and Dox/NR incubation ratio was varied from 100 to 5 \times 10⁵:1. In both cases, [PhB] was fixed at 10 mM.

Calculation of the Aggregation Index (AI). NRs' stability was quantified as an aggregation index (AI).³⁵ The AI is a measure of the longitudinal surface plasmon resonance (LSPR) peak broadening derived from the total area under the absorption spectrum of the LSPR from 600 to 900 nm, divided by LSPR intensity. The AI gives the equivalent bandwidth of the longitudinal peak (with units of nanometer) for a spectrum normalized to the LSPR peak intensity. A higher degree of aggregation corresponds to a higher AI value.

Triggered Release of Payloads from NR-ES. Samples were prepared in 10 mM PhB at a DNA/NR and Dox/NR incubation ratio of 2000:1 and 10⁵:1, respectively, before being irradiated by a pulsed femtosecond laser that outputs a 1 kHz train of 100 fs pulses at 790 nm (fwhm = 16 nm, 600 mW) (Spectral Physics, Inc.). Then, 200 mW of the output with a spot size of 6 mm was used to irradiate 100 μ L of NR-ES-DNA/Dox in 3 \times 3 mm quartz cuvette (Starna Cells) from 0 to 15 min, with regular pipetting at 3 min interval for even irradiation of the sample. The amount of ES proteins, DNA, and Dox released was quantified by fluorescence as described earlier in the quantification of payloads on

NR-ES. Laser irradiation was repeated for samples with varying [PhB] and incubation ratios as described earlier.

Leakage of Payloads from NR-ES-DNA/Dox. To determine the payload leakage with time, 1 nM of NR-ES-DNA/Dox (10 mM PhB, DNA/NR ratio = 5000:1 and Dox/NR ratio = 10⁵:1) was left at standard room condition for 14 days. At set time points, 100 μ L of the samples was centrifuged at 11 000 rpm for 10 min to isolate the fluorescent payload and ES proteins that had leaked into the supernatant from the NR pellet. Quantification of the leaked DNA, Dox, and ES proteins was by fluorescence.

Conflict of Interest: The authors declare no competing financial interest.

Acknowledgment. Funding was from the NSF (DMR #0906838). J.C.Y.K. was supported by the NUS OPF; A.Z. was supported by the NSF Research Experience for Undergraduates (REU) program. We thank Zhichuan Xu for TEM imaging, and the MIT Center for Materials Science and Engineering for use of the TEM. We thank the Tokmakoff group for use of their laser, and the Bawendi group for use of their zetasizer.

Supporting Information Available: Additional data on the release of ES proteins, NR absorption spectra, loading and release efficiencies, leakage efficiencies and fluorescence measurements. This material is available free of charge via the Internet at <http://pubs.acs.org>.

REFERENCES AND NOTES

- Kah, J. C. Y.; Olivo, M.; Chow, T. H.; Song, K. S.; Koh, K. Z. Y.; Mhaisalkar, S.; Sheppard, C. J. R. Control of Optical Contrast Using Gold Nanoshells for Optical Coherence Tomography Imaging of Mouse Xenograft Tumor Model *in Vivo*. *J. Biomed. Opt.* **2009**, *14*, 054015.
- Li, P. C.; Wang, C. R. C.; Shieh, D. B.; Wei, C. W.; Liao, C. K.; Poe, C.; Jhan, S.; Ding, A. A.; Wu, Y. N. *In Vivo* Photoacoustic Molecular Imaging with Simultaneous Multiple Selective Targeting Using Antibody-Conjugated Gold Nanorods. *Opt. Express* **2008**, *16*, 18605–18615.
- Park, H.; Lee, S.; Chen, L.; Lee, E. K.; Shin, S. Y.; Lee, Y. H.; Son, S. W.; Oh, C. H.; Song, J. M.; Kang, S. H.; *et al.* SERS Imaging of HER2-Overexpressed MCF7 Cells Using Antibody-Conjugated Gold Nanorods. *Phys. Chem. Chem. Phys.* **2009**, *11*, 7444–7449.
- Gupta, S.; Andresen, H.; Ghadiali, J. E.; Stevens, M. M. Kinase-Actuated Immunoaggregation of Peptide-Conjugated Gold Nanoparticles. *Small* **2010**, *6*, 1509–1513.
- Liu, X.; Dai, Q.; Austin, L.; Coutts, J.; Knowles, G.; Zou, J. H.; Chen, H.; Huo, Q. A One-Step Homogeneous Immunoassay for Cancer Biomarker Detection Using Gold Nanoparticle Probes Coupled with Dynamic Light Scattering. *J. Am. Chem. Soc.* **2008**, *130*, 2780–2782.
- Goodrich, G. P.; Bao, L. L.; Gill-Sharp, K.; Sang, K. L.; Wang, J.; Payne, J. D. Photothermal Therapy in a Murine Colon Cancer Model Using Near-Infrared Absorbing Gold Nanorods. *J. Biomed. Opt.* **2010**, *15*, 018001.
- Huang, X. H.; El-Sayed, I. H.; El-Sayed, M. A. Applications of Gold Nanorods for Cancer Imaging and Photothermal Therapy. *Cancer Nanotechnol.* **2010**, *624*, 343–357.
- Wijaya, A.; Schaffer, S. B.; Pallares, I. G.; Hamad-Schifferli, K. Selective Release of Multiple DNA Oligonucleotides from Gold Nanorods. *ACS Nano* **2009**, *3*, 80–86.
- Agarwal, A.; Mackey, M. A.; El-Sayed, M. A.; Bellamkonda, R. V. Remote Triggered Release of Doxorubicin in Tumors by Synergistic Application of Thermosensitive Liposomes and Gold Nanorods. *ACS Nano* **2011**, *5*, 4919–4926.
- Niidome, T.; Ohga, A.; Akiyama, Y.; Watanabe, K.; Niidome, Y.; Mori, T.; Katayama, Y. Controlled Release of PEG Chain from Gold Nanorods: Targeted Delivery to Tumor. *Bioorg. Med. Chem.* **2010**, *18*, 4453–4458.
- Yamashita, S.; Fukushima, H.; Akiyama, Y.; Niidome, Y.; Mori, T.; Katayama, Y.; Niidome, T. Controlled-Release System of Single-Stranded DNA Triggered by the Photothermal Effect of Gold Nanorods and Its *In Vivo* Application. *Bioorg. Med. Chem.* **2011**, *19*, 2130–2135.

12. Chen, C.-C.; Lin, Y.-P.; Wang, C.-W.; Tzeng, H.-C.; Wu, C.-H.; Chen, Y.-C.; Chen, C.-P.; Chen, L.-C.; Wu, Y.-C. DNA-Gold Nanorod Conjugates for Remote Control of Localized Gene Expression by Near-Infrared Irradiation. *J. Am. Chem. Soc.* **2006**, *128*, 3709–3715.
13. Arvizo, R. R.; Rana, S.; Miranda, O. R.; Bhattacharya, R.; Rotello, V. M.; Mukherjee, P. Mechanism of Anti-Angiogenic Property of Gold Nanoparticles: Role of Nanoparticle Size and Surface Charge. *Nanomed. Nanotech. Biol. Med.* **2011**, *7*, 580–587.
14. Eum, N. S.; Yeom, S. H.; Kwon, D. H.; Kim, H. R.; Kang, S. W. Enhancement of Sensitivity Using Gold Nanorods-Antibody Conjugator for Detection of *E. coli* O157:H7. *Sens. Actuators, B* **2010**, *143*, 784–788.
15. Rostro-Kohanloo, B. C.; Bickford, L. R.; Payne, C. M.; Day, E. S.; Anderson, L. J. E.; Zhong, M.; Lee, S.; Mayer, K. M.; Zal, T.; Adam, L.; *et al.* The Stabilization and Targeting of Surfactant-Synthesized Gold Nanorods. *Nanotechnology* **2009**, *20*, 434005.
16. Wijaya, A.; Hamad-Schifferli, K. Ligand Customization and DNA Functionalization of Gold Nanorods via Round-Trip Phase Transfer Ligand Exchange. *Langmuir* **2008**, *24*, 9966–9969.
17. Pissuwan, D.; Nose, K.; Kurihara, R.; Kaneko, K.; Tahara, Y.; Kamiya, N.; Goto, M.; Katayama, Y.; Niidome, T. A Solid-in-Oil Dispersion of Gold Nanorods Can Enhance Transdermal Protein Delivery and Skin Vaccination. *Small* **2011**, *7*, 215–220.
18. Lynch, I.; Salvati, A.; Dawson, K. A. Protein–Nanoparticle Interactions: What Does the Cell See? *Nat. Nanotechnol.* **2009**, *4*, 546–547.
19. Cedervall, T.; Lynch, I.; Lindman, S.; Berggard, T.; Thulin, E.; Nilsson, H.; Dawson, K. A.; Linse, S. Understanding the Nanoparticle–Protein Corona Using Methods to Quantify Exchange Rates and Affinities of Proteins for Nanoparticles. *Proc. Natl. Acad. Sci. U.S.A.* **2007**, *104*, 2050–2055.
20. Lynch, I.; Dawson, K. A. Protein–Nanoparticle Interactions. *Nano Today* **2008**, *3*, 40–47.
21. Mahmoudi, M.; Lynch, I.; Ejtehadi, M. R.; Monopoli, M. P.; Bombelli, F. B.; Laurent, S. Protein–Nanoparticle Interactions: Opportunities and Challenges. *Chem. Rev.* **2011**, *111*, 5610–5637.
22. Monopoli, M. P.; Walczyk, D.; Campbell, A.; Elia, G.; Lynch, I.; Baldelli Bombelli, F.; Dawson, K. A. Physical–Chemical Aspects of Protein Corona: Relevance to *In Vitro* and *In Vivo* Biological Impacts of Nanoparticles. *J. Am. Chem. Soc.* **2011**, *133*, 2525–2534.
23. Safi, M.; Courtois, J.; Seigneuret, M.; Conjeaud, H.; Berret, J. F. The Effects of Aggregation and Protein Corona on the Cellular Internalization of Iron Oxide Nanoparticles. *Biomaterials* **2011**, *32*, 9353–9363.
24. de Puig, H.; Federici, S.; Baxamusa, S. H.; Bergese, P.; Hamad-Schifferli, K. Quantifying the Nanomachinery of the Nanoparticle–Biomolecule Interface. *Small* **2011**, *7*, 2477–2484.
25. Gref, R.; Lück, M.; Queller, P.; Marchand, M.; Dellacherie, E.; Harnisch, S.; Blunk, T.; Müller, R. H. 'Stealth' Corona-Core Nanoparticles Surface Modified by Polyethylene Glycol (PEG): Influences of the Corona (PEG Chain Length and Surface Density) and of the Core Composition on Phagocytic Uptake and Plasma Protein Adsorption. *Colloids Surf., B* **2000**, *18*, 301–313.
26. Maiorano, G.; Sabella, S.; Sorce, B.; Brunetti, V.; Malvindi, M. A.; Cingolani, R.; Pompa, P. P. Effects of Cell Culture Media on the Dynamic Formation of Protein–Nanoparticle Complexes and Influence on the Cellular Response. *ACS Nano* **2010**, *4*, 7481–7491.
27. Casals, E.; Pfaller, T.; Duschl, A.; Oostingh, G. J.; Püntes, V. Time Evolution of the Nanoparticle Protein Corona. *ACS Nano* **2010**, *4*, 3623–3632.
28. Lindman, S.; Lynch, I.; Thulin, E.; Nilsson, H.; Dawson, K. A.; Linse, S. Systematic Investigation of the Thermodynamics of HSA Adsorption to *N*-iso-Propylacrylamide/*N*-tert-Butylacrylamide Copolymer Nanoparticles. Effects of Particle Size and Hydrophobicity. *Nano Lett.* **2007**, *7*, 914–920.
29. Dell'Orco, D.; Lundqvist, M.; Oslakovic, C.; Cedervall, T.; Linse, S. Modeling the Time Evolution of the Nanoparticle–Protein Corona in a Body Fluid. *PLoS ONE* **2010**, *5*, e10949.
30. Marchi, N.; Betto, G.; Fazio, V.; Fan, Q.; Ghosh, C.; Machado, A.; Janigro, D. Blood-Brain Barrier Damage and Brain Penetration of Antiepileptic Drugs: Role of Serum Proteins and Brain Edema. *Epilepsia* **2009**, *50*, 664–677.
31. Hamberger, C.; Barre, J.; Zini, R.; Taiclet, A.; Houin, G.; Tillement, J. P. *In Vitro* Binding Study of Gemfibrozil to Human-Serum Proteins and Erythrocytes: Interactions with Other Drugs. *Int. J. Clin. Pharm. Res.* **1986**, *6*, 441–449.
32. Israeli, Z.; Wilson, C. H. The Binding of Drugs to Human-Serum Proteins. *Clin. Res.* **1983**, *31*, A651–A651.
33. Jeong, H.; Huh, M.; Lee, S. J.; Koo, H.; Kwon, I. C.; Jeong, S. Y.; Kim, K. Photosensitizer-Conjugated Human Serum Albumin Nanoparticles for Effective Photodynamic Therapy. *Theranostics* **2011**, *1*, 230–239.
34. Thong, P. S. P.; Olivo, M.; Chin, W. W. L.; Bhuvanewari, R.; Mancner, K.; Soo, K. C. Clinical Application of Fluorescence Endoscopic Imaging Using Hypericin for the Diagnosis of Human Oral Cavity Lesions. *Br. J. Cancer* **2009**, *101*, 1580–1584.
35. Dreis, S.; Rothweiler, F.; Michaelis, A.; Cinatl, J.; Kreuter, J.; Langer, K. Preparation, Characterisation and Maintenance of Drug Efficacy of Doxorubicin-Loaded Human Serum Albumin (HSA) Nanoparticles. *Int. J. Pharm.* **2007**, *341*, 207–214.
36. Kufleitner, J.; Wagner, S.; Worek, F.; von Briesen, H.; Kreuter, J. Adsorption of Obidoxime onto Human Serum Albumin Nanoparticles: Drug Loading, Particle Size and Drug Release. *J. Microencapsulation* **2010**, *27*, 506–513.
37. Steinhäuser, I. M.; Langer, K.; Strebhardt, K. M.; Spänkuch, B. Effect of Trastuzumab-Modified Antisense Oligonucleotide-Loaded Human Serum Albumin Nanoparticles Prepared by Heat Denaturation. *Biomaterials* **2008**, *29*, 4022–4028.
38. Fischer, D.; Bieber, T.; Brüsselbach, S.; Elsässer, H. P.; Kissel, T. Cationized Human Serum Albumin as a Non-viral Vector System for Gene Delivery? Characterization of Complex Formation with Plasmid DNA and Transfection Efficiency. *Int. J. Pharm.* **2001**, *225*, 97–111.
39. Simoes, S.; Slepishkin, V.; Pires, P.; Gaspar, R.; de Lima, M. C. P.; Duzgunes, N. Human Serum Albumin Enhances DNA Transfection by Lipoplexes and Confers Resistance to Inhibition by Serum. *Biochim. Biophys. Acta* **2000**, *1463*, 459–469.
40. Brewer, S. H.; Glomm, W. R.; Johnson, M. C.; Knag, M. K.; Franzen, S. Probing BSA Binding to Citrate-Coated Gold Nanoparticles and Surfaces. *Langmuir* **2005**, *21*, 9303–9307.
41. Bajaj, A.; Samanta, B.; Yan, H.; Jerry, D. J.; Rotello, V. M. Stability, Toxicity and Differential Cellular Uptake of Protein Passivated-Fe₃O₄ Nanoparticles. *J. Mater. Chem.* **2009**, *19*, 6328–6331.
42. Hurst, S. J.; Lytton-Jean, A. K. R.; Mirkin, C. A. Maximizing DNA Loading on a Range of Gold Nanoparticle Sizes. *Anal. Chem.* **2006**, *78*, 8313–8318.
43. Albanese, A.; Chan, W. C. W. Effect of Gold Nanoparticle Aggregation on Cell Uptake and Toxicity. *ACS Nano* **2011**, *5*, 5478–5489.
44. Sethi, M.; Joung, G.; Knecht, M. R. Stability and Electrostatic Assembly of Au Nanorods for Use in Biological Assays. *Langmuir* **2009**, *25*, 317–325.
45. Prapainop, K.; Witter, D. P.; Wentworth, P. A Chemical Approach for Cell-Specific Targeting of Nanomaterials, Small Molecule-Initiated Misfolding of Nanoparticle Corona Proteins. *J. Am. Chem. Soc.* **2012**, *134*, 4100–4103.
46. Dell'Orco, D.; Lundqvist, M.; Cedervall, T.; Linse, S. Delivery Success Rate of Engineered Nanoparticles in the Presence of the Protein Corona: A Systems-Level Screening. *Nanomedicine: Nanotechnology, Biology and Medicine* **2012**, DOI: 10.1016/j.nano.2012.02.006.
47. De, M.; Rana, S.; Akpınar, H.; Miranda, O. R.; Arvizo, R. R.; Bunz, U. H. F.; Rotello, V. M. Sensing of Proteins in Human

- Serum Using Conjugates of Nanoparticles and Green Fluorescent Protein. *Nat. Chem.* **2009**, *1*, 461–465.
48. Arvizo, R. R.; Giri, K.; Moyano, D.; Miranda, O. R.; Madden, B.; McCormick, D. J.; Bhattacharya, R.; Rotello, V. M.; Kocher, J.-P.; Mukherjee, P. Identifying New Therapeutic Targets via Modulation of Protein Corona Formation by Engineered Nanoparticles. *PLoS ONE* **2012**, *7*, e33650.
 49. Takahashi, H.; Niidome, Y.; Yamada, S. Controlled Release of Plasmid DNA from Gold Nanorods Induced by Pulsed Near-Infrared Light. *Chem. Commun.* **2005**, 2247–2249.
 50. Huschka, R.; Zuloaga, J.; Knight, M. W.; Brown, L. V.; Nordlander, P.; Halas, N. J. Light-Induced Release of DNA from Gold Nanoparticles: Nanoshells and Nanorods. *J. Am. Chem. Soc.* **2011**, *133*, 12247–12255.
 51. Sau, T. K.; Murphy, C. J. Seeded High Yield Synthesis of Short Au Nanorods in Aqueous Solution. *Langmuir* **2004**, *20*, 6414–6420.
 52. Alkilany, A. M.; Nalaria, P. K.; Hexel, C. R.; Shaw, T. J.; Murphy, C. J.; Wyatt, M. D. Cellular Uptake and Cytotoxicity of Gold Nanorods: Molecular Origin of Cytotoxicity and Surface Effects. *Small* **2009**, *5*, 701–708.
 53. Niidome, T.; Yamagata, M.; Okamoto, Y.; Akiyama, Y.; Takahashi, H.; Kawano, T.; Katayama, Y.; Niidome, Y. PEG-Modified Gold Nanorods with a Stealth Character for *In Vivo* Applications. *J. Controlled Release* **2006**, *114*, 343–347.
 54. Lazarides, A. A.; Schatz, G. C. DNA-Linked Metal Nanosphere Materials: Structural Basis for the Optical Properties. *J. Phys. Chem. B* **2000**, *104*, 460–467.
 55. Kah, J. C.-Y.; Zubieta, A.; Saavedra, R. A.; Hamad-Schifferli, K. Stability of Gold Nanorods Passivated with Amphiphilic Ligands. *Langmuir* **2012**, *28*, 8834–8844.
 56. Ogris, M.; Brunner, S.; Schüller, S.; Kircheis, R.; Wagner, E. PEGylated DNA/Transferrin-PEI Complexes: Reduced Interaction with Blood Components, Extended Circulation in Blood and Potential for Systemic Gene Delivery. *Gene Ther.* **1999**, *6*, 595–605.
 57. Park, S.; Brown, K. A.; Hamad-Schifferli, K. Changes in Oligonucleotide Conformation on Nanoparticle Surfaces by Modification with Mercaptohexanol. *Nano Lett.* **2004**, *4*, 1925–1929.
 58. Demers, L. M.; Mirkin, C. A.; Mucic, R. C.; Reynolds, R. A., III; Letsinger, R. L.; Elghanian, R.; Viswanadham, G. A Fluorescence-Based Method for Determining the Surface Coverage and Hybridization Efficiency of Thiol-Capped Oligonucleotides Bound to Gold Thin Films and Nanoparticles. *Anal. Chem.* **2000**, *72*, 5535–5541.
 59. Hill, H. D.; Millstone, J. E.; Banholzer, M. J.; Mirkin, C. A. The Role Radius of Curvature Plays in Thiolated Oligonucleotide Loading on Gold Nanoparticles. *ACS Nano* **2009**, *3*, 418–424.
 60. Poon, Z.; Chang, D.; Zhao, X.; Hammond, P. T. Layer-by-Layer Nanoparticles with a pH-Sheddable Layer for *In Vivo* Targeting of Tumor Hypoxia. *ACS Nano* **2011**, *5*, 4284–4292.
 61. Yoo, D.; Shiratori, S. S.; Rubner, M. F. Controlling Bilayer Composition and Surface Wettability of Sequentially Adsorbed Multilayers of Weak Polyelectrolytes. *Macromolecules* **1998**, *31*, 4309–4318.
 62. Aryal, S.; Grailer, J. J.; Pilla, S.; Steeber, D. A.; Gong, S. Doxorubicin Conjugated Gold Nanoparticles as Water-Soluble and pH-Responsive Anticancer Drug Nanocarriers. *J. Mater. Chem.* **2009**, *19*, 7879–7884.
 63. Prabakaran, M.; Grailer, J. J.; Pilla, S.; Steeber, D. A.; Gong, S. Gold Nanoparticles with a Monolayer of Doxorubicin-Conjugated Amphiphilic Block Copolymer for Tumor-Targeted Drug Delivery. *Biomaterials* **2009**, *30*, 6065–6075.
 64. Fang, B.; Gon, S.; Park, M.; Kumar, K. N.; Rotello, V. M.; Nusslein, K.; Santore, M. M. Bacterial Adhesion on Hybrid Cationic Nanoparticle-Polymer Brush Surfaces: Ionic Strength Tunes Capture from Monovalent to Multivalent Binding. *Colloids Surf., B* **2011**, *87*, 109–115.
 65. Chen, K.; Xu, Y.; Rana, S.; Miranda, O. R.; Dubin, P. L.; Rotello, V. M.; Sun, L.; Guo, X. Electrostatic Selectivity in Protein–Nanoparticle Interactions. *Biomacromolecules* **2011**, *12*, 2552–2561.
 66. Seyrek, E.; Dubin, P. L.; Tribet, C.; Gamble, E. A. Ionic Strength Dependence of Protein–Polyelectrolyte Interactions. *Biomacromolecules* **2003**, *4*, 273–282.
 67. Link, S.; Burda, C.; Nikoobakht, B.; El-Sayed, M. A. Laser-Induced Shape Changes of Colloidal Gold Nanorods Using Femtosecond and Nanosecond Laser Pulses. *J. Phys. Chem. B* **2000**, *104*, 6152–6163.
 68. Khee Chaw, N.; Wenlong, C. Fine-Tuning Longitudinal Plasmon Resonances of Nanorods by Thermal Reshaping in Aqueous Media. *Nanotechnology* **2012**, *23*, 105602.
 69. Ekici, O.; Harrison, R. K.; Durr, N. J.; Eversole, D. S.; Lee, M.; Ben-Yakar, A. Thermal Analysis of Gold Nanorods Heated with Femtosecond Laser Pulses. *J. Phys. D: Appl. Phys.* **2008**, *41*, 185501.
 70. You, J.; Zhang, G. D.; Li, C. Exceptionally High Payload of Doxorubicin in Hollow Gold Nanospheres for Near-Infrared Light-Triggered Drug Release. *ACS Nano* **2010**, *4*, 1033–1041.
 71. Grabinski, C.; Schaeublin, N.; Wijaya, A.; D'Couto, H.; Baxamusa, S. H.; Hamad-Schifferli, K.; Hussain, S. M. Effect of Gold Nanorod Surface Chemistry on Cellular Response. *ACS Nano* **2011**, *5*, 2870–2879.
 72. Ferhan, A. R.; Guo, L.; Kim, D.-H. Influence of Ionic Strength and Surfactant Concentration on Electrostatic Surface Assembly of Cetyltrimethylammonium Bromide-Capped Gold Nanorods on Fully Immersed Glass. *Langmuir* **2010**, *26*, 12433–12442.
 73. Leonov, A. P.; Zheng, J.; Clogston, J. D.; Stern, S. T.; Patri, A. K.; Wei, A. Detoxification of Gold Nanorods by Treatment with Polystyrenesulfonate. *ACS Nano* **2008**, *2*, 2481–2488.
 74. Alper, J. D.; Crespo, M.; Hamad-Schifferli, K. Release Mechanism of Octadecyl Rhodamine B Chloride from Au Nanorods by Ultrafast Laser Pulses. *J. Phys. Chem. C* **2009**, *113*, 5967–5973.
 75. Gole, A.; Murphy, C. J. Polyelectrolyte-Coated Gold Nanorods: Synthesis, Characterization and Immobilization. *Chem. Mater.* **2005**, *17*, 1325–1330.